Tunable long-lived exciton lifetime in single-layer two-dimensional $LiAlTe_2$

Hao Dong (董昊),* Jinfeng Zhao (赵金峰),† Huan Yang (杨欢),‡ and Yujun Zheng (郑雨军)§
School of Physics, Shandong University, Jinan 250100, China

(Received 6 December 2021; accepted 23 September 2022; published 10 October 2022)

In two-dimensional (2D) materials, Coulomb interactions induce large binding energies of excitons, which are detrimental to the charge separations and hence crucial to photovoltaic performance. Here, we elucidate that this drawback can be well restrained in 2D materials with an intrinsic polarization field. Based on first-principles calculations combined with nonadiabatic molecular dynamics, we propose an embodied example of a $LiAlTe_2$ quadruple layer. Due to the inherent electrical polarization field in 2D $LiAlTe_2$, the electron and hole wave functions are separated into opposite atomic layers similar to the case of heterostructures, reducing the undesired Coulomb interactions and contributing to the small binding energy of excitons. Through modeling and recording the excited-state dynamics, we reveal that 2D $LiAlTe_2$ harbors an ultralong lifetime of excitons of about 1.69 ns, a recombination time that is similar to that found in type-II van der Waals heterostructures and superior to hitherto known 2D photovoltaic components. Furthermore, the effect of strain on the electron-hole recombination is studied quantitatively. Our findings not only provide a compelling candidate for applications in wearable and flexible thin-film solar cells, but also suggest one of the possible ways to design the thin-film solar cells.

DOI: 10.1103/PhysRevMaterials.6.104001

I. INTRODUCTION

Applicable materials for solar cells are of great importance for energy-harvesting technologies [1–3]. Recently, tremendous efforts have been made to achieve ultrathin photovoltaics based on two-dimensional (2D) materials, to meet the high demand for next-generation wearable and flexible energy devices. Examples mainly include graphene, 2D transition metal dichalcogenides (TMDs), and 2D perovskite [4–8]. However, these 2D photovoltaic materials generally yield a power conversion efficiency (PCE) between approximately 1 and 15%, which is far behind what is needed for commercial popularization. To enhance their PCEs, various engineering technologies have been proposed, such as introducing defects, a heterointerface, and ligands, to suppress carrier recombination [4,5,9]. Although these external means can indeed enhance their PCEs, the required conditions are complicated and far from controllable. To this end, searching for 2D photovoltaic materials potentially with intrinsically high PCEs [10–13] is essentially crucial for developing excellent solar cells.

Janus materials have also stimulated intensive research in recent years due to their rich physics. The innate polarization field renders Janus materials promising platforms for gas sensors, multiferroics, piezoelectric energy harvesting, catalysts, and optoelectronics [14,15]. A step further, the inversion symmetry breaking gives birth to the quantum-confined Stark effect and thus can introduce a slope to the energy bands and separate electrons from holes, which has been experimentally validated in GaAs/AlGaAs quantum wells (QWs) [16], InGaN QWs [17], and CdSe-CdS colloidal quantum dots [18]. Very recently, a largely decreased binding energy of excitons has been observed in solution-processed layered hybrid perovskites as a result of dipolar polarizability of methylammonium cations [19]. The intrinsic polarization field in 2D materials leads to the spatial separation of electrons and holes and ultimately results in the modulation of band structures [20,21]. Cudazzo *et al.* showed a correlation between binding energies and electron-hole overlap, namely, that the binding energies are always high irrespective of the degree of localization of the electron-hole wave function, in these typical 2D materials including graphene, phosphorene, and hexagonal boron nitride (BN) [22]. However, in Janus-type materials, the intrinsic electric field is built under the quantum Stark effect, and the reduced overlap of the electron-hole wave function is expected to suppress the possibility of transition of excited electrons to the valence band, which will improve the charge carrier lifetime significantly. Stemming from these innovations, one may wonder whether it is possible to find ultrathin 2D materials with a long timescale of the exciton lifetime for efficient solar cells by utilizing the Stark effect. Currently, however, this design strategy has scarcely been reported in 2D fields, and only a few candidates have been proposed [23].

The 2D $LiAlTe_2$ may serve as one such candidate. In 2000, Kim and Hughbanks synthesized two types of bulk $LiAlTe_2$ with different crystal structures, namely, α-$LiAlTe_2$ and β-$LiAlTe_2$ [24]. Inspired by the layered structure of β-$LiAlTe_2$, in 2019, Liu *et al.* found the novel 2D structure γ-$LiAlTe_2$ according to their first-principles calculations and

*Present address: Hebei Key Laboratory of Physics and Energy Technology, Department of Mathematics and Physics, North China Electric Power University, Baoding 071003, China.
†Present address: Institute of Molecular Sciences and Engineering, Institute of Frontier and Interdisciplinary Science, Shandong University, Qingdao 266237, China; jfzhao1990112@163.com
‡h.yang@sdu.edu.cn
§yzheng@sdu.edu.cn

investigated the out-of-plane and in-plane piezoelectricity in 2D Li-based ternary chalcogenides LiMX_2 [25]. In 2021, Mak *et al.* studied the electronic and spin properties driven by spin-orbit coupling and found a large and tunable Rashba spin splitting in γ-LiAlTe$_2$ [26]. In 2022, Qiu *et al.* systematically studied the piezoelectric properties of 2D LiAlTe$_2$ and found that the piezoelectric coefficients are highly adjustable by strain and stacking [27].

By means of first principles and nonadiabatic molecular dynamics, we herein show that single-layer 2D LiAlTe$_2$ is indeed such a promising candidate with a tunable long-lived exciton lifetime. The existing intrinsic polarization field in 2D LiAlTe$_2$ can produce the desired properties of small exciton binding energy and thus ultralong exciton lifetime. This indicates one of the possible ways to design next-generation wearable and flexible 2D solar cells. Considering the durability against strain in 2D LiAlTe$_2$, we also present a reasonable modulation manner to achieve desirable carrier selective contacts with metals, and this could enhance the performance of solar cells.

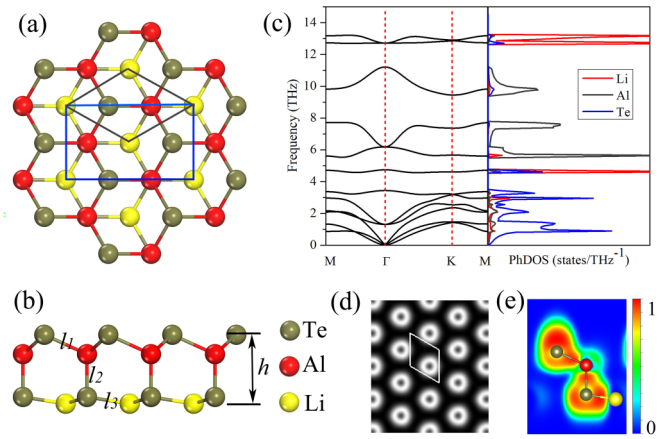

FIG. 1. (a) Top and (b) side views of the crystal structure of 2D LiAlTe$_2$. The rectangular (triangular) unit cell is marked with blue (gray) solid lines. Te-Al and Te-Li bonds are labeled with l_1, l_2, and l_3. (c) Phonon dispersion curves (left) and the corresponding partial phonon density of states (PhDOS) (right) of LiAlTe$_2$. (d) Simulated STM image for 2D LiAlTe$_2$. (e) Electron localization function (ELF) map of 2D LiAlTe$_2$ along planes containing specified bonding atoms.

II. METHODS

A. Details of *ab initio* calculations

The structural optimization, *ab initio* molecular dynamics (AIMD) simulation, and ground-state band structure calculations are performed using the Vienna *ab initio* simulation package [28]. The generalized gradient approximation of Perdew, Burke, and Ernzerhof (PBE) is used for the exchange-correlation potential [29]. The projector-augmented wave (PAW) [28] method with a cutoff energy of 500 eV is adopted. Structures are fully relaxed until energy and forces are converged to 10^{-5} eV and 0.01 eV/Å, respectively. The Brillouin zone integration is sampled with Monkhorst-Pack k-point meshes of $9 \times 9 \times 1$. A vacuum space larger than 20 Å is used to avoid the interactions between its periodic images. The van der Waals–D3 (vdW-D3) method is employed to better describe the interlayer dispersion interactions in bulk LiAlTe$_2$ [30]. To accurately describe the band gap and exciton binding energy, the Hedin's GW approximation and Bethe-Salpeter equation (GW-BSE) formalism and the Heyd-Scuseria-Ernzerhof (HSE) hybrid function, including 25% Fock exchange and 75% PBE exchange, are adopted. The dielectric functions including electron-hole interactions are computed by solving the BSE using the YAMBO code [31]. The electronic band structures from density functional theory are corrected by G_0W_0 quasiparticle (QP) energies using 300 empty bands, and a $36 \times 36 \times 1$ k grid is adopted for G_0W_0 and BSE calculations. Phonon spectra are calculated using a $5 \times 5 \times 1$ supercell with PHONOPY [32]. The coefficients of the relaxed-ion elastic stiffness tensor and piezoelectric tensor e_{ijk} are obtained by using density functional perturbation theory (DFPT) [33].

B. Crystal structure and stability

Bulk β-LiAlTe$_2$ (space group $P3m1$) has been synthesized and possesses polar layers akin to the isostructural LiMnTe$_2$ [24,34]. Its crystal structure is provided in the Appendix, and the optimized lattice constants are 4.33 and 7.22 Å for the a and c axes, which are in good agreement with experiments. In bulk LiAlTe$_2$, the interlayers are combined with van der Waals forces, and the interlayer distance according to our calculations is 2.90 Å. According to a recent theoretical study, bulk materials with this range of interlayer distance have the possibility to be exfoliated [35]. The crystal structure of 2D LiAlTe$_2$ is displayed in Figs. 1(a) and 1(b). It can be seen that 2D LiAlTe$_2$ exhibits a quadruple layer structure. The lattice constant and layer thickness h are found to be 4.39 and 4.10 Å, respectively. The bond lengths are found to be 2.78, 2.54, and 2.56 Å for l_1, l_2, and l_3, respectively. Due to its uneven top and bottom surfaces, it shows an innate polarization field of 0.36 D per unit cell normal to the basal plane. To confirm its dynamical stability, we calculate its phonon spectra. As shown in Fig. 1(c), all phonon branches (three acoustical and nine optical) are real in the entire Brillouin zone, suggesting the dynamical stability of 2D LiAlTe$_2$. Furthermore, we can see that the high-frequency modes are contributed from Li atoms, Te atoms dominate frequency modes below 4 THz, and the contribution from Al atoms is mainly between approximately 5 and 12 THz. This arises from the fact that the lighter the atom is, the higher the vibrational energy is. Besides, the highest phonon frequency, 13.19 THz (440 cm^{-1}), is comparable to those of MoS$_2$ (473 cm^{-1}) [36] and silicene (550 cm^{-1}) [37], indicating that its chemical bonds are comparatively robust. The AIMD simulations for the thermal stability examination of 2D LiAlTe$_2$ are supplied in the Appendix; from these simulations it can be found that the total energies remain almost invariant and 2D LiAlTe$_2$ retains its structural integrity without bonds being broken or lattice reconstruction throughout a 7.5-ps simulation at 300 K. These pieces of evidence clearly point out the high structural stability of 2D LiAlTe$_2$ for potential applications.

To facilitate the experimental study, a simulated scanning tunneling microscopy (STM) image of 2D LiAlTe$_2$ from the top view is shown in Fig. 1(d). Bright areas denote the sites

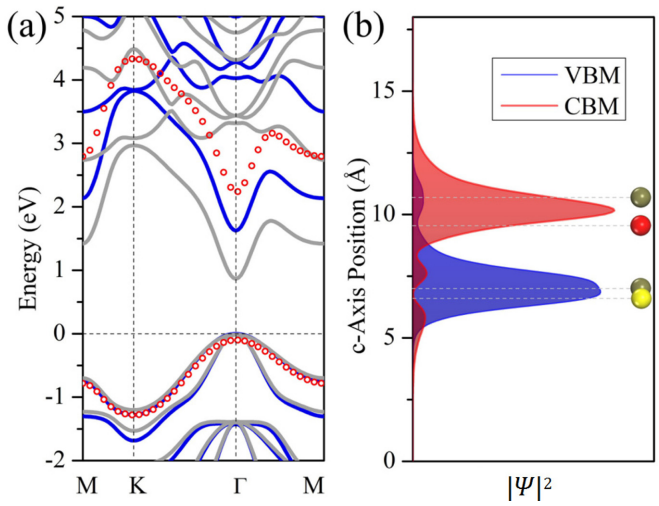

FIG. 2. (a) Band structures of 2D $LiAlTe_2$ using PBE (gray lines) and HSE06 (blue lines) functionals. The red open circles represent the QP-corrected energies. (b) Electron and hole wave functions squared for 2D $LiAlTe_2$.

of Te atoms, forming a honeycomb STM pattern. To get insight into the chemical bond classification in 2D $LiAlTe_2$, its electron localization function (ELF) is calculated and shown in Fig. 1(e). ELF could be used to analyze the extent of spatial localization of a referenced electron, while the upper limit $\mathrm{ELF}(r) = 1$ represents perfect localization and $\mathrm{ELF}(r) = 1/2$ for electron-gas-like pairs. It is found that an appreciable number of electrons distribute in the middle region of Li-Te and Al-Te, indicating the strong covalent electron states.

III. RESULTS AND DISCUSSION

A. Electronic and optical properties

The band structure of 2D $LiAlTe_2$ is shown in Fig. 2(a). 2D $LiAlTe_2$ is a direct band gap semiconductor, with both the conduction band minimum (CBM) and valence band maximum (VBM) locating at the Γ point. There are double-degenerate states at the VBM. The band gap is found to be 0.88 eV (PBE) and 1.62 eV (HSE), which is close to other plausible photovoltaic candidates, such as KAgSe [38], trilayer silicene [13], and black phosphorus (BP) [39]. The moderate value of the band gap suggests that 2D $LiAlTe_2$ holds great potential for applications in photovoltaics (PVs) and optoelectronics (more details about the electronic properties are supplied in the Appendix).

The electronic states near the Fermi level are mainly contributed by Te-p orbitals. From the electron and hole wave functions shown in Fig. 2(b), we found that the CBM originates from the top layers of Al and Te, while the VBM is contributed by the bottom layers of Te and Li. This is attributed to the strong vertical intrinsic polarization field induced by its asymmetric structure, which causes the atomic energy levels of the top and bottom layers to be staggered. One may wonder whether this electronic property favors optical transition. According to the dipole transition matrix elements [40] between the band edges which are shown in the Appendix, no parity-forbidden transition between the lowest conduction band and the topmost valence band is observed, and especially large transition matrix elements around the Γ point are observed, revealing a high transition probability within them. Thus such a unique dipole-allowed electronic ground state generally favors a reduced Coulomb interaction as the electron and hole are becoming spatially separated. This has the benefit of decreasing their recombination probability and thus is highly desirable for PV candidates.

It is known that the excited electrons and holes tend to present in pairs as a result of the Coulomb force, referred to as quasiparticles (QPs) [41]. The electron-hole pairs (excitonic effects) would influence the corresponding optical properties. To explore the excitonic effect in 2D $LiAlTe_2$, we conduct GW calculations to obtain its QP band gap and optical band gap. As shown in Fig. 2(a), the band gap of 2D $LiAlTe_2$ is 2.32 eV locating at the Γ point at the G_0W_0 level, which is 0.70 eV larger than that at the HSE06 level. The prominent excitonic effects are particularly important for the low-energy optical response and the charge carrier dynamics of the ultrathin materials. The imaginary part of the dielectric function

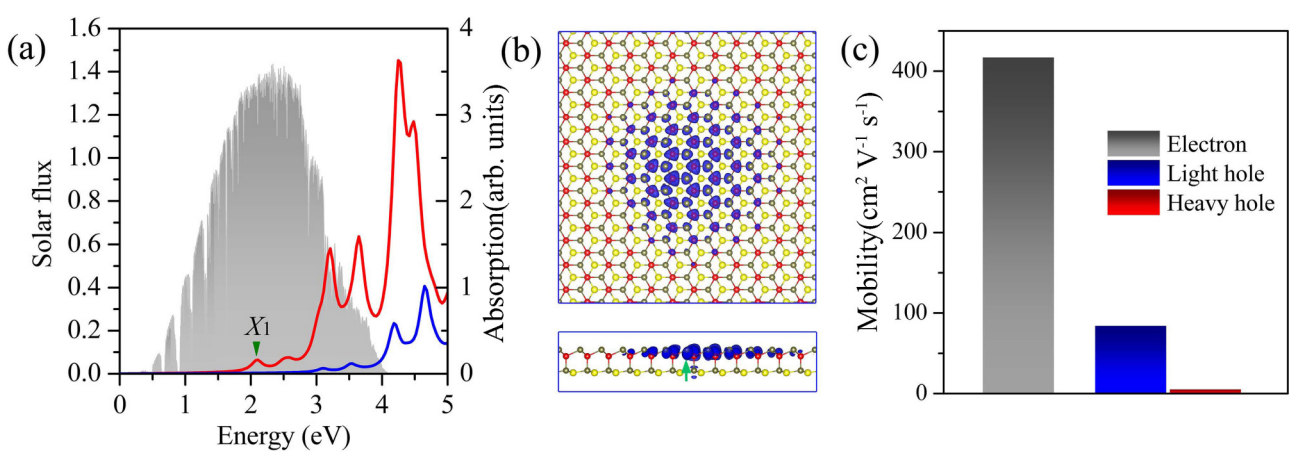

FIG. 3. (a) Optical absorption spectra of 2D $LiAlTe_2$ superimposed on the incident AM1.5G solar flux (gray area). The red and blue lines are the spectra with GW-BSE and GW-RPA, respectively. (b) Probability distribution of electrons in real space for the lowest-energy exciton (X1) in 2D $LiAlTe_2$ with a fixed hole position marked with a green arrow. (c) The charge carrier mobility of 2D $LiAlTe_2$.

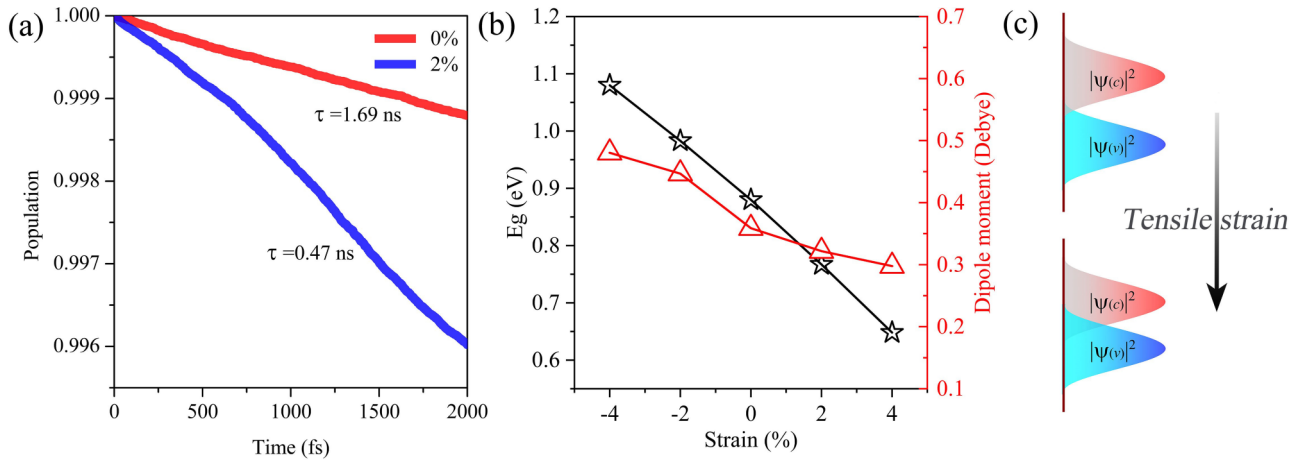

FIG. 4. (a) Electron-hole recombination dynamics in 2D $LiAlTe_2$ at 300 K under 0 and 2% biaxial strain. (b) Evolution of band gap and surface dipole moment as a function of biaxial strain. (c) Schematic plot of squared functions of electron and hole for 2D $LiAlTe_2$ under 0 and biaxial tensile strain.

that determines optical absorption is expressed in terms of excitonic states [42], as

$$\epsilon_2(\hbar\omega) \propto \sum_S \left| \sum_{cv\mathbf{k}} A^S_{cv\mathbf{k}} \frac{\langle c\mathbf{k} \mid p_i \mid v\mathbf{k}\rangle}{\epsilon_{c\mathbf{k}} - \epsilon_{v\mathbf{k}}} \right|^2 \delta(\Omega^S - \hbar\omega). \quad (1)$$

Based on the solution of the BSE with excitonic effects, the absorption spectrum of 2D $LiAlTe_2$ is obtained and shown in Fig. 3(a) as a red line. In Fig. 3(a), the spectrum of the random phase approximation (RPA) on top of the QP corrections (GW-RPA) is also shown for comparison. Clearly, we can observe the large overlap between the absorption spectra and the incident AM1.5G (air mass 1.5 global) solar flux, which suggests that 2D $LiAlTe_2$ hosts the ability for visible and ultraviolet light absorption when applying it in solar cells. Despite all that, as a result of spatially separated electrons and holes, the first absorption peak close to the maximum of the solar spectrum is not that strong. In addition, the first prominent optical absorption peak (X1, defined as the optical band gap) for the 2D $LiAlTe_2$ monolayer locates at 2.11 eV [Fig. 3(a)], corresponding to the bright exciton at the Γ point with binding energies E_b of 0.21 eV. This value is much smaller than those of 2D boron dichalcogenides (above 1 eV) [41], BP (0.8 eV) [43], GeSe (0.4 eV) [44], and TMDs (0.65 eV) [45] and is even comparable to that of organic-inorganic hybrid perovskite nanosheets (0.20 eV) [46]. By accessing the wave function of the X1 exciton, we find that the electronic part of the wave function solely localizes in the top Al-Te sublayer when the hole is placed in the bottom Li-Te sublayer [Fig. 3(b)]. So the creation of such an exciton corresponds to the charge transfer from the bottom Li-Te layer to the top Al-Te layer. The charge transfer and less overlap of electron and hole wave functions clearly indicate the charge-separated feature and therefore the small E_b. These findings reveal the behavior of the photoexcited charge carriers in 2D $LiAlTe_2$ and make it an ideal candidate for PV applications.

The carrier mobility μ of the material, influencing the operation speed of electronic devices, is also a crucial parameter in determining the performance for optoelectronic applications. We then estimate the carrier mobility of single-layer 2D $LiAlTe_2$ at room temperature in the framework of deformation potential (DP) theory, proposed by Bardeen and Shockley [47]. The analytical expression of acoustic-phonon-limited carrier mobility in 2D materials can be written as

$$\mu_{2D} = \frac{2e\hbar^3 C_{2D}}{3K_B T |m^*|^2 E_d^2}, \quad (2)$$

where e, $\hbar$, K_B, T, $m*$, C_{2D}, and E_d stand for the electron charge, reduced Planck constant, Boltzmann constant, room temperature (300 K), effective masses, elastic modulus, and DP constant, respectively. The results are shown in Fig. 3(c), and detailed information is provided in the Appendix. The predicted carrier mobility for an electron is

TABLE I. The calculated relaxed-ion elastic tensor C_{kj} in units of N/m, piezoelectric tensor e_{ij} in 10^{-10} pC/m, and piezoelectric coefficients d_{ik} in pm/V.

Material	C_{11}	C_{12}	e_{11}	e_{31}	d_{11}	d_{31}
$LiAlTe_2$	38.21	17.26	0.91	0.62	4.33	1.13
$LiAlTe_2$ [25]	37.77	16.10	0.99	0.45	4.58	0.83
$LiAlTe_2$ [27]	37.47	15.71	81.12[a]	51.55[a]	3.73	0.97
$LiAlTe_2$ [72]	39.9	17.1				
Janus MoSSe [73]	126.8	27.4	3.74	0.032	3.76	0.02
MoS2 [74]	130	32	3.64		3.73	

[a]The units of e_{ik} given in Table 1 of Ref. [27] appear to be a typo and may be pC/m as indicated in Fig. 5(b) of the same reference.

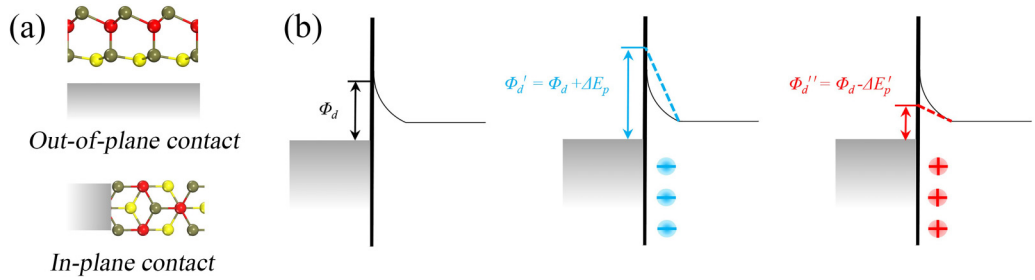

FIG. 5. (a) Schematic in-plane and out-of-plane contacts with metal. (b) Band diagrams explaining the result of the changes in Schottky barrier heights by strain-induced polarization. Φ_d and ΔE_p indicate the Schottky barrier formed at the pristine 2D-$LiAlTe_2$–metal contact and the change in Schottky barrier height by piezoelectric polarization charges, respectively.

0.417×10^3 cm^2 V^{-1} s^{-1}, while the hole mobility is found to be 0.005×10^3 and 0.084×10^3 cm^2 V^{-1} s^{-1} for heavy and light holes, respectively. The carrier mobility of 2D $LiAlTe_2$ is roughly comparable to that of many other 2D materials [15,48,49]. Such high carrier mobilities also enable 2D $LiAlTe_2$ to be a promising material for efficient thin-film flexible solar cells. The electron mobility is higher than the hole mobility suggesting that the 2D $LiAlTe_2$ is likely to be an n-type semiconductor. Additionally, the large discrepancy between electron and hole mobility (more than one order of magnitude) also reflects its remarkable ability for electron and hole separation. We should emphasize that the mobility calculations, often adopted in the literature, are simply based on elastic tensors and deformation potentials, which cannot account for scattering on optical phonons. Xu *et al.* reported an electron mobility greater than 10^3 cm^2 V^{-1} s^{-1} in their study of Li-based ternary chalcogenides [50]. Nevertheless, we provide here an estimation of mobility, mainly to compare 2D $LiAlTe_2$ with other 2D materials investigated in the literature within the same level of theory.

B. Electron-hole recombination dynamics and strain effects

In the above analysis, we estimate the recombination probability of excited states qualitatively, and we believe this process should be quite slow. To be more specific, the lifetime of photogenerated carriers is quantitatively evaluated using time domain density functional theory combined with nonadiabatic molecular dynamics (NAMD). PYXAID [51] and HEFEI-NAMD [52] are two popular programs performing NAMD simulations. Recently, excitonic effects were taken into account using a method developed by Akimov and coworkers [53,54] and by the Zhao group [55]. Considering some unknown effects and the computational cost, here the PYXAID program based on the single-particle picture [56,57] is employed to investigate the real-time relaxation dynamics of the photoexcited states. Previous NAMD investigations for various condensed matter systems, such as a TiO_2 quantum dot, a metal cluster-semiconductor, and 2D monolayers, justify this method [58,59]. Starting from the time-dependent Schrödinger equation and Kohn-Sham (KS) orbitals [57],

$$i\hbar\frac{\partial}{\partial t}\Psi_n(\mathbf{r},t) = H(\mathbf{r},\mathbf{R},t)\Psi_n(\mathbf{r},t), \tag{3}$$

$$\Psi_n(\mathbf{r},t) = \sum_\alpha C_\alpha^n(t)\Phi_\alpha(\mathbf{r};\mathbf{R}(t)), \tag{4}$$

the probability of transition between adiabatic states j and k can be obtained by employing the consensus surface hopping method [60,61]. After photon excitation, a free electron and hole formed in the CBM and VBM, respectively. Meanwhile, nonradiative decay of the lowest excited electronic state leads to recovery of the population for the ground state, i.e., a free charge recombination process. Assuming that the full decay process is exponential [62], the relaxation time τ is fitted to be 1.69 ns as shown in Fig. 4(a), according to

$$P(t) = \exp\left(-\frac{t}{\tau}\right). \tag{5}$$

Meanwhile, we found that the obtained recombination time is one order of magnitude larger than that of 2D TMDs (hundreds of picoseconds), and even two orders of magnitude larger than that of BP (57 ps) [59]. Such long-lived excited

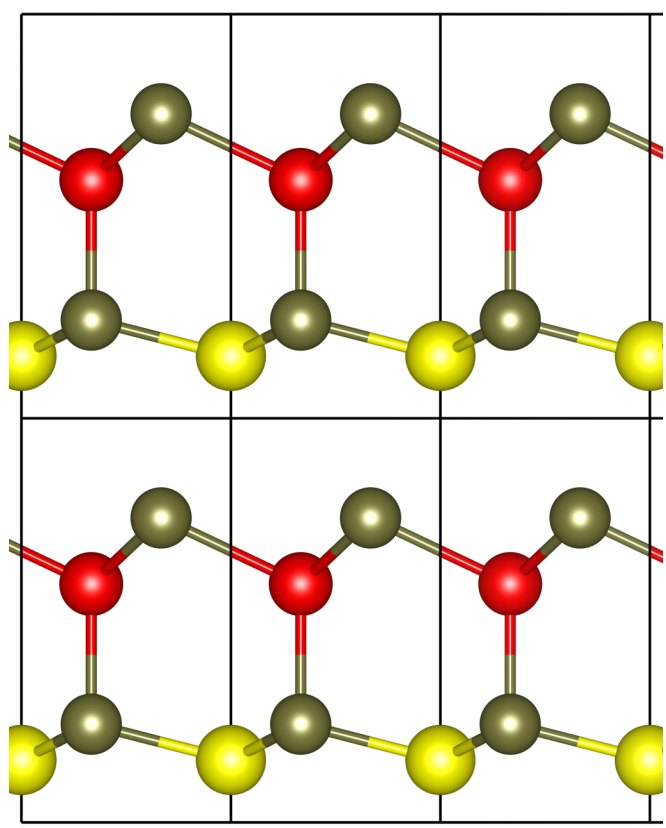

FIG. 6. Crystal structure of bulk $LiAlTe_2$.

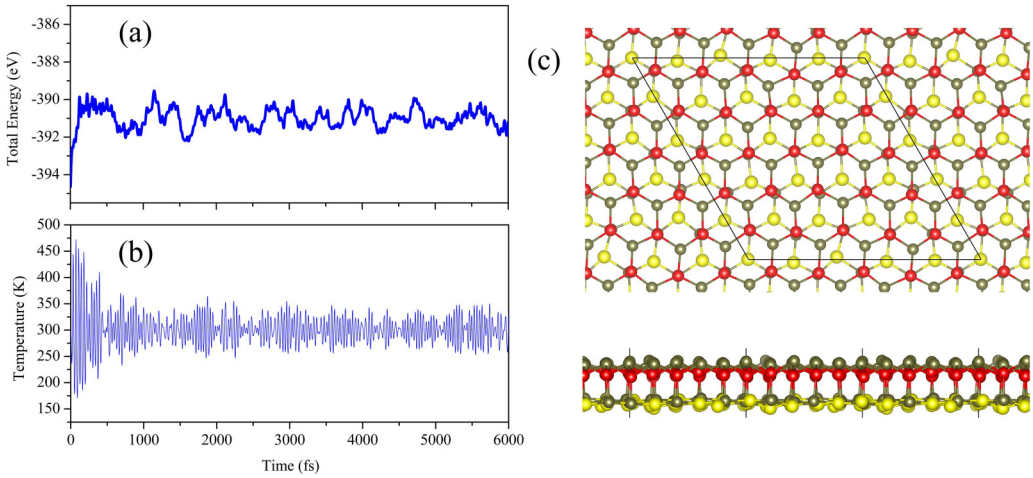

FIG. 7. Fluctuation of (a) total energy and (b) temperature with time obtained from molecular dynamics (MD) simulation of a $LiAlTe_2$ monolayer at 300 K. (c) Snapshot of 2D $LiAlTe_2$ at the end of MD simulation at 300 K from top and side views.

carriers are even comparable to a TMD type-II van der Waals heterostructure [63]. This long lifetime of excited states is mainly the result of its electronic feature, as the polarization field pushes an electron and hole to be localized in different domains of the structure, thus producing a much reduced Coulomb interaction and weak nonadiabatic coupling (NAC). The resultant weak NAC favors slower nonradiative decay as it determines the hopping probability of hot electrons from one state to another [52,64]. Such an ultralong timescale for electron-hole recombination strongly suggests its potential applications in next-generation optoelectronic and thin-film PVs with high PCE. It should be mentioned that the charge recombination time may be further prolonged by increasing the thickness of the film, as the magnitude of polarization will be elevated and free carriers would be transferred separately to the outermost monolayers, and this would suppress the recombination [65,66].

In 2D materials, strain can be easily introduced experimentally by a lattice mismatch on the substrate or by mechanical loading [67]. Thus one may wonder how 2D $LiAlTe_2$ responds to mechanical deformation. We investigate this problem by introducing $-4\% \longrightarrow 4\%$ external biaxial strain. The evolution of the surface dipole moment, PBE band structures, and band gap as a function of applied strain are shown in Fig. 4(b) (see the Appendix for more details). We can see that the surface dipole moment decreases from 0.48 D to 0.29 D monotonously with increasing strain from -4% to 4%, resulting from charge redistribution and changes of thickness within $LiAlTe_2$ when the lattice is stretched or compressed. As for the electronic structure, we found that the band gap undergoes a decreasing trend as the biaxial tensile strain increases. The band gap increases to 1.08 eV under 4% compressive strain, while the band gap decreases to 0.65 eV under 4% tensile strain. It should be noted that its character of a direct band gap is robust against strain within the range of $\pm 4\%$. It is found that tensile strain decreases both the band gap and the surface dipole moment, so we also investigated how it influences charge recombination. The electron-hole recombination dynamics in single-layer 2D $LiAlTe_2$ under 2% biaxial tensile strain is included in Fig. 4(a), and the simulated decay time of excited electrons decreased to 0.47 ns. This can be rationalized by the fact that compressive (tensile) strain enlarges (reduces) the layer thickness of 2D $LiAlTe_2$, which is calculated to be 4.28 Å (3.99 Å) under a strain of -2% (2%). The facts of decreased innate polarization field and decreased layer thickness at 2% tensile strain increase the overlap of electron $[|\Psi(c)|^2]$ and hole wave functions $[|\Psi(v)|^2]$ [as schematically described in Fig. 4(c)]. Accompanied with a narrowed band gap, this gives rise to stronger NAC, which is verified by the calculated NAC of 2.12 meV (2.73 meV) at a strain of 0% (2%), thus leading to faster charge recombination. In this respect, experimentally and carefully modulating the properties of 2D $LiAlTe_2$ via strain is vital.

C. In-plane and out-of-plane piezoelectricities

Currently, piezophototronic solar cells are attracting enormous research interest [68–71]. Due to the absence of an inversion center and mirror symmetry, both in-plane and out-of-plane piezoelectric effects are allowed. Finally, we discuss the piezoelectricity of the 2D $LiAlTe_2$ monolayer. In the 2D limit, the relaxed-ion piezoelectric tensor e_{ij} is the sum of the ionic tensor e_{ij}^{ion} and the electronic tensor e_{ij}^{el}. The relation between the piezoelectric tensor, the piezoelectric coefficients d_{ik}, and the elastic tensor C_{kj} obeys $e_{ij} = d_{ik}C_{kj}$; the Einstein

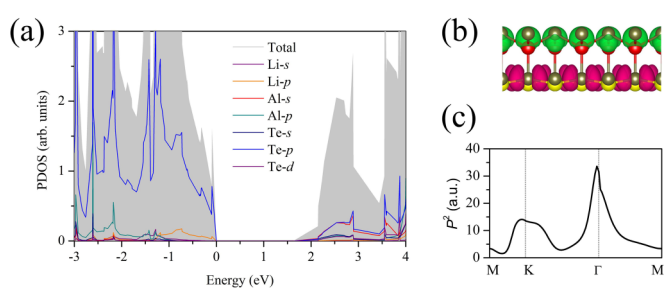

FIG. 8. (a) Projected density of states (PDOS) and (b) real-space orbital plot of CBM (green area) and VBM (red region) for a $LiAlTe_2$ monolayer. The isosurface level is set to be 0.04 $e/\text{Å}^3$. (c) Calculated dipole transition matrix elements.

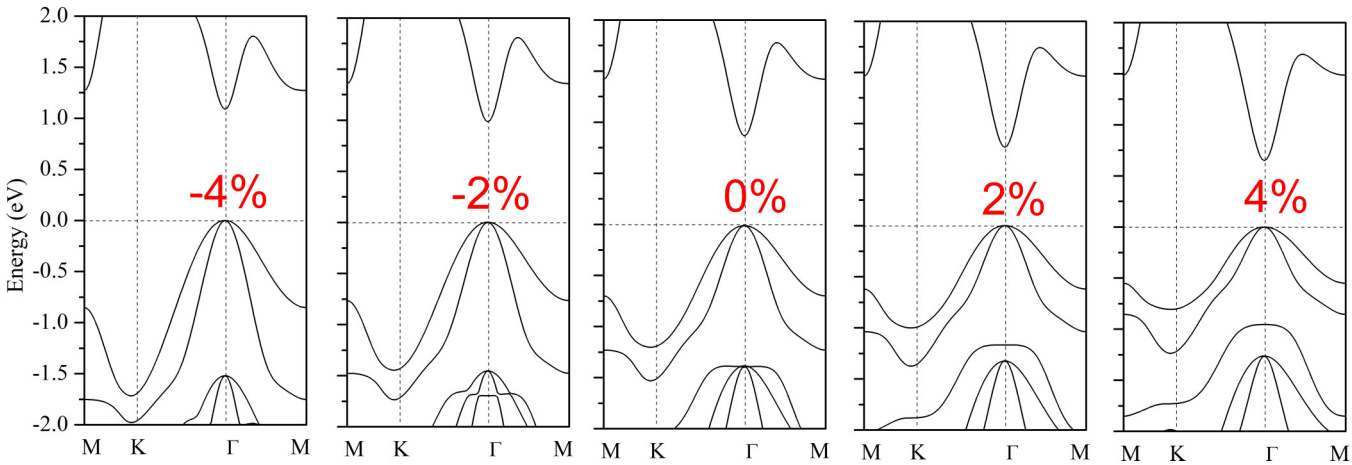

FIG. 9. Variations of electronic band structures for a $LiAlTe_2$ monolayer with strains.

summation convention is used here. Together with C_{3V} symmetry, for hexagonal $LiAlTe_2$ the in-plane and out-of-plane coefficients satisfy [73]

$$d_{11} = \frac{e_{11}}{C_{11} - C_{12}}, \quad d_{31} = \frac{e_{31}}{C_{11} + C_{12}}. \tag{6}$$

As listed in Table I, the value of e_{11} for $LiAlTe_2$ is 0.91×10^{-10} C/m, smaller than that of Janus MoSSe and MoS_2, but the value of e_{31} is comparatively larger, reaching 0.62×10^{-10} C/m. The corresponding piezoelectric coefficients d_{11} and d_{31} are found to be 4.33 and 1.13 pm/V; both are larger than those of Janus MoSSe and MoS_2. Due to the fact that $LiAlTe_2$ is remarkably less stiff, these values indicate a larger mechanical-electrical energy conversion ratio in both in-plane and out-of-plane directions. We note that massive efforts have been made to search for 2D piezoelectric materials with large d_{31} (known examples include Janus-TMDs [73], oxygen functionalized MXenes (a class of transition metal carbides or nitrides) [14], decorated graphene [75], and α-In_2Se_3 [76]), but d_{31} values are still very small and thus not appealing. However, these values are adjustable by strain and stacking [27].

The especially strong out-of-plane piezoelectric effect in 2D $LiAlTe_2$ is thus more suitable for ultrathin cantilever and diaphragm devices [14], compared with the aforementioned hitherto known 2D systems. It is also an important factor that one can comprehend and optimize the operation of constructed PVs. Considering the durability against strain in 2D $LiAlTe_2$, the high piezoelectric coefficients allow another opportunity for utilizing the polarity of the piezopotential to tune the in-plane and out-of-plane interfacial charge transport [68,77], such as effective Schottky barriers. Two possible approaches for 2D-$LiAlTe_2$–metal contacts are shown in Fig. 5(a), that is, vertically stacked or in-plane linked with a metal electrode. Via proper structural deformations, the distribution of carriers in 2D $LiAlTe_2$ could be modified, and the electronic charges in interface states could be modulated, where the mechanical strain functions as a controlling gate signal. Piezoelectric polarization charges distribute at the surface, which may affect the electrical transport properties across the whole contact area formed between 2D $LiAlTe_2$ and metal. Thus, here we present a reasonable modulation manner to achieve desirable carrier selective contacts with metals [Fig. 5(b)]. It could promote the probability of carrier collection per absorbed photon and hence enhance the performance of solar cells [9,71,78].

IV. CONCLUSION

In summary, we report the realization of spatially separated electrons and holes in single-layer 2D $LiAlTe_2$ under the condition of an innate internal polarization field. The material itself innately hosts properties that otherwise require cumbersome treatment to be induced in 2D materials. As the consequence, reduction of the Coulomb interaction is expected and hence the accelerated exciton dissociation and collection. This is confirmed by the ultralong lifetime (1.69 ns) of electron-hole recombination. The advanced properties, namely, the moderate band gap, compelling optical property, high mobility, appreciable in-plane and out-of-plane piezoelectric effects, and weakly bounded excitons with long-timescale recombination, suggest that 2D $LiAlTe_2$ is one promising material for ultrathin-film photovoltaic applications. Besides, the design strategy described here will be applicable to other elements to yield more 2D materials with outstanding electronic properties and functionalities for high-PCE PVs.

ACKNOWLEDGMENTS

This work was supported by the National Natural Science Foundation of China (Grants No. 12174221 and No. 11674196). H.Y. is grateful for the support of the Taishan Scholars Project of Shandong Province (Grant No. ts201712011). Calculations were performed in part at the Micro-modular Data Platform of the School of Physics at Shandong University.

TABLE II. Carrier effective masses m^*, elastic modulus C, deformation potential constants E_d, and carrier mobilities μ of monolayer $LiAlTe_2$.

Carrier type	m^*/m_0	C (N/m)	E_d (eV)	μ (cm^2 V^{-1} s^{-1})
Electron	0.15		7.99	0.417×10^3
Heavy hole	1.37	41.187	7.88	0.005×10^3
Light hole	0.34		7.75	0.084×10^3

TABLE III. Lattice parameters and atomic coordinates of $LiAlTe_2$.

	X	Y	Z
	Lattice parameters		
	3.803	−2.196	0.000
	0.000	4.391	0.000
	0.000	0.000	18.150
	Atomic coordinates		
Li	1.000	0.000	0.102
Al	0.333	0.667	0.264
Te	0.333	0.667	0.124
Te	0.667	0.333	0.327

APPENDIX: ADDITIONAL DETAILS OF CALCULATIONS, FIGURES, AND TABLES

In this paper, the *GW* calculations are performed using the YAMBO code interfaced with QUANTUM ESPRESSO [79]. The KS orbitals are expanded with a cutoff of 80 Ry in kinetic energy, a k-point mesh of $9 \times 9 \times 1$ is used for Brillouin zone sampling, and the Kohn-Sham–density-functional-theory (KS-DFT) charge density and wave function were adopted as the starting point for calculating the QP self-energy and BSE two-particle Green's function [80]. In the above calculations, the semicore electrons are described by the Troullier-Martins pseudopotential [81], and spin is not included as the system studied here is not spin polarized.

Four additional figures and two more tables are supplied in this Appendix. They show the crystal structure of bulk $LiAlTe_2$ (Fig. 6); fluctuations of total energy and temperature and snapshots of 2D $LiAlTe_2$ at 300 K from top and side views (Fig. 7); the projected density of states, real-space orbital plot of CBM and VBM for a $LiAlTe_2$ monolayer, and dipole transition matrix elements (Fig. 8); variations of electronic band structures for $LiAlTe_2$ monolayer with strains (Fig. 9); parameters used to calculate the carrier mobility (Table II); and lattice parameters as well as the atomic coordinates (Table III).

[1] N. J. Jeon, J. H. Noh, W. S. Yang, Y. C. Kim, S. Ryu, J. Seo, and S. Seok, Nature (London) **517**, 476 (2015).
[2] J. Ramanujam and U. P. Singh, Energy Environ. Sci. **10**, 1306 (2017).
[3] W. Wu, Y. Xu, J. Liao, L. Wang, and D. Kuang, Nano Energy **62**, 791 (2019).
[4] C. Tan, X. Cao, X. Wu, Q. He, J. Yang, X. Zhang, J. Chen, W. Zhao, S. Han, G. H. Nam, M. Sindoro, and H. Zhang, Chem. Rev. **117**, 6225 (2017).
[5] A. J. Cho, M. K. Song, D. W. Kang, and J. Y. Kwon, ACS Appl. Mater. Interfaces **10**, 35972 (2018).
[6] M. Bernardi, M. Palummo, and J. C. Grossman, Nano Lett. **13**, 3664 (2013).
[7] B. Febriansyah, T. M. Koh, Y. Lekina, N. F. Jamaludin, A. Bruno, R. Ganguly, Z. X. Shen, S. G. Mhaisalkar, and J. England, Chem. Mater. **31**, 890 (2019).
[8] A. H. Proppe, R. Quintero-Bermudez, H. Tan, O. Voznyy, S. O. Kelley, and E. H. Sargent, J. Am. Chem. Soc. **140**, 2890 (2018).
[9] D. Jariwala, A. R. Davoyan, J. Wong, and H. A. Atwater, ACS Photonics **4**, 2962 (2017).
[10] C. Zhang, Y. Nie, S. Sanvito, and A. Du, Nano Lett. **19**, 1366 (2019).
[11] Y. Guo, Q. Wu, Y. Li, N. Lu, K. Mao, Y. Bai, J. Zhao, J. Wang, and X. C. Zeng, Nanoscale Horiz. **4**, 223 (2019).
[12] S. Guo, W. Zhou, B. Cai, K. Zhang, S. Zhang, and H. Zeng, Nanoscale Horiz. **4**, 1145 (2019).
[13] J. Lv, M. Xu, S. Lin, X. Shao, X. Zhang, Y. Liu, Y. Wang, Z. Chen, and Y. Ma, Nano Energy **51**, 489 (2018).
[14] J. Tan, Y. Wang, Z. Wang, X. He, Y. Liu, B. Wang, M. I. Katsnelson, and S. Yuan, Nano Energy **65**, 104058 (2019).
[15] X. Ma, X. Wu, H. Wang, and Y. Wang, J. Mater. Chem. A **6**, 2295 (2018).
[16] H. J. Polland, L. Schultheis, J. Kuhl, E. O. Gobel, and C. W. Tu, Phys. Rev. Lett. **55**, 2610 (1985).
[17] E. Kioupakis, Q. Yan, and C. G. Van de Walle, Appl. Phys. Lett. **101**, 231107 (2012).
[18] B. C. Pein, W. Chang, H. Y. Hwang, J. Scherer, I. Coropceanu, X. Zhao, X. Zhang, V. Bulovic, M. Bawendi, and K. A. Nelson, Nano Lett. **17**, 5375 (2017).
[19] G. Walters, M. Wei, O. Voznyy, R. Quintero-Bermudez, A. Kiani, D. M. Smulgies, R. Munur, A. Amassian, S. Hoogland, and E. Sargent, Nat. Commun. **9**, 4214 (2018).
[20] D. Zhang, W. Lou, M. Miao, S. C. Zhang, and K. Chang, Phys. Rev. Lett. **111**, 156402 (2013).
[21] M. S. Miao, Q. Yan, C. G. Van de Walle, W. K. Lou, L. L. Li, and K. Chang, Phys. Rev. Lett. **109**, 186803 (2012).
[22] P. Cudazzo, L. Sponza, C. Giorgetti, L. Reining, F. Sottile, and M. Gatti, Phys. Rev. Lett. **116**, 066803 (2016).
[23] N. Sanders, D. Bayerl, G. Shi, K. A. Mengle, and E. Kioupakis, Nano Lett. **17**, 7345 (2017).
[24] J. Kim and T. Hughbanks, Inorg. Chem. **39**, 3092 (2000).
[25] S. Liu, W. Chen, C. Liu, B. Wang, and H. Yin, Results Phys. **26**, 104398 (2021).
[26] K. Y. Mak, L. L. Tao, and Y. Zhou, Appl. Phys. Lett. **118**, 062404 (2021).
[27] J. Qiu, X. Chen, F. Zhang, B. B. Zhu, H. Guo, X. Liu, J. Yu, and J. Bao, Nanotechnology **33**, 055702 (2022).
[28] P. E. Blöchl, Phys. Rev. B **50**, 17953 (1994).
[29] J. P. Perdew and A. Zunger, Phys. Rev. B **23**, 5048 (1981).
[30] S. Grimme, J. Antony, S. Ehrlich, and H. Krieg, J. Chem. Phys. **132**, 154104 (2010).
[31] S. Mann, P. Rani, R. Kumar, and V. K. Jindal, AIP Conf. Proc. **1675**, 030035 (2015).
[32] A. Marini, C. Hogan, M. Grüning, and D. Varsano, Comput. Phys. Commun. **180**, 1392 (2009).
[33] X. Wu, D. Vanderbilt, and D. R. Hamann, Phys. Rev. B **72**, 035105 (2005).
[34] L. Isaenko, I. Vasilyeva, A. Merkulov, A. Yelisseyev, and S. Lobanov, J. Cryst. Growth **275**, 217 (2005).
[35] Z. Liu, Y. Sun, D. J. Singh, and L. Zhang, Adv. Electron. Mater. **5**, 1900089 (2019).

[36] A. Molina-Sánchez and L. Wirtz, Phys. Rev. B **84**, 155413 (2011).
[37] S. Cahangirov, M. Topsakal, E. Akturk, H. Sahin, and S. Ciraci, Phys. Rev. Lett. **102**, 236804 (2009).
[38] Q. Wang, J. Li, Y. Liang, Y. Nie, and B. Wang, ACS Appl. Mater. Interfaces **10**, 41670 (2018).
[39] J. Qiao, X. Kong, Z. X. Hu, F. Yang, and W. Ji, ACS Appl. Mater. Interfaces **5**, 4475 (2014).
[40] W. Meng, X. Wang, Z. Xiao, J. Wang, D. B. Mitzi, and Y. Yan, J. Phys. Chem. Lett. **8**, 2999 (2017).
[41] C. Tang, F. Ma, C. Zhang, Y. Jiao, S. K. Matta, K. Ostrikov, and A. Du, J. Mater. Chem. C **7**, 1651 (2019).
[42] E. Torun, H. P. C. Miranda, A. Molina-Sánchez, and L. Wirtz, Phys. Rev. B **97**, 245427 (2018).
[43] V. Tran, R. Soklaski, Y. Liang, and L. Yang, Phys. Rev. B **89**, 235319 (2014).
[44] L. C. Gomes, P. E. Trevisanutto, A. Carvalho, A. S. Rodin, and A. H. Castro Neto, Phys. Rev. B **94**, 155428 (2016).
[45] M. M. Ugeda, A. J. Bradley, S.-F. Shi, F. H. da Jornada, Y. Zhang, D. Y. Qiu, W. Ruan, S. K. Mo, Z. Hussain, Z. Shen, F. Wang, S. G. Louie, and M. F. Crommie, Nat. Mater. **13**, 1091 (2014).
[46] Q. Zhang, L. Chu, F. Zhou, W. Ji, and G. Eda, Adv. Mater. **30**, 1704055 (2018).
[47] J. Bardeen and W. Shockley, Phys. Rev. **80**, 72 (1950).
[48] W. Zhou, S. Guo, S. C. Zhang, Z. Zhu, X. Song, T. Niu, K. Zhang, X. Liu, Y. Zou, and H. Zeng, Nanoscale **10**, 3350 (2018).
[49] Y. L. Liu, Y. Shi, H. Yin, and C. L. Yang, Appl. Phys. Lett. **117**, 063901 (2020).
[50] W. Xu, R. Wang, B. Zheng, X. Wu, and H. Xu, J. Phys. Chem. Lett. **10**, 6061 (2019).
[51] R. Long, J. Liu, and O. V. Prezhdo, J. Am. Chem. Soc. **138**, 3884 (2016).
[52] Q. Zheng, W. Chu, C. Zhao, L. Zhang, H. Guo, Y. Wang, X. Jiang, and J. Zhao, WIREs Comput. Mol. Sci. **9**, e1411 (2019).
[53] B. Smith, M. Shakiba, and A. V. Akimov, J. Chem. Theory Comput. **17**, 678 (2021).
[54] B. Smith, M. Shakiba, and A. V. Akimov, J. Phys. Chem. Lett. **12**, 2444 (2021).
[55] X. Jiang, Q. Zheng, Z. Lan, W. A. Saidi, X. Ren, and J. Zhao, Sci. Adv. **7**, eabf3759 (2021).
[56] A. Akimov and O. Prezhdo, J. Chem. Theory Comput. **9**, 4959 (2013).
[57] A. V. Akimov and O. V. Prezhdo, J. Chem. Theory Comput. **10**, 789 (2014).
[58] L. Wang, R. Long, and O. Prezhdo, Annu. Rev. Phys. Chem. **66**, 549 (2015).
[59] R. Long, M. Guo, L. Liu, and W. Fang, J. Phys. Chem. Lett. **7**, 1830 (2016).
[60] C. C. Martens, J. Phys. Chem. Lett. **7**, 2610 (2016).
[61] C. C. Martens, J. Phys. Chem. A **123**, 1110 (2019).
[62] S. Wang, Q. Luo, W. H. Fang, and R. Long, J. Phys. Chem. Lett. **10**, 1234 (2019).
[63] L. Li, R. Long, and O. V. Prezhdo, Chem. Mater. **29**, 2466 (2017).
[64] L. Zhang, A. S. Vasenko, J. Zhao, and O. V. Prezhdo, J. Phys. Chem. Lett. **10**, 1083 (2019).
[65] A. C. Riis Jensen, M. Pandey, and K. S. Thygesen, J. Phys. Chem. C **122**, 24520 (2018).
[66] Y. Li, Q. Cui, F. Ceballos, S. D. Lane, Z. Qi, and H. Zhao, Nano Lett. **17**, 6661 (2017).
[67] X. Zhu, F. Li, Y. Wang, M. Qiao, and Y. Li, J. Mater. Chem. C **6**, 4494 (2018).
[68] J. Sun, Q. Hua, R. Zhou, D. Li, W. Guo, X. Li, G. Hu, C. Shan, Q. Meng, L. Dong, C. Pan, and Z. L. Wang, ACS Nano **13**, 4507 (2019).
[69] S. Qiao, J. Liu, G. Fu, K. Ren, Z. Li, S. Wang, and C. Pan, Nano Energy **49**, 508 (2018).
[70] C. Jiang, Y. Chen, J. Sun, L. Jing, M. Liu, T. Liu, Y. Pan, X. Pu, B. Ma, W. Hu, and Z. L. Wang, Nano Energy **57**, 300 (2019).
[71] D. Q. Zheng, Z. Zhao, R. Huang, J. Nie, L. Li, and Y. Zhang, Nano Energy **32**, 448 (2017).
[72] Z. Wang, Y. Pan, T. Li, K. Wu, T. Rao, L. Hu, Y. Feng, and C. Yang, Phys. B (Amsterdam) **626**, 413531 (2022).
[73] L. Dong, J. Lou, and V. B. Shenoy, ACS Nano **11**, 8242 (2017).
[74] K. A. N. Duerloo, M. T. Ong, and E. J. Reed, J. Phys. Chem. Lett. **3**, 2871 (2012).
[75] M. T. Ong and E. J. Reed, ACS Nano **6**, 1387 (2012).
[76] L. Hu and X. Huang, RSC Adv. **7**, 55034 (2017).
[77] W. Wu, L. Wang, Y. Li, F. Zhang, L. Lin, S. Niu, D. Chenet, X. Zhang, Y. Hao, T. F. Heinz, J. Hone, and Z. L. Wang, Nature (London) **514**, 470 (2014).
[78] P. Lin, C. Pan, and Z. Wang, Mater. Today **4**, 17 (2018).
[79] P. Giannozzi, S. Bonini, B. Nicola, M. Calandra, R. Car, C. Cavazzoni, D. Ceresoli, G. L. Chiarotti, M. Cococcioni, I. Dabo, and A. Dal Corso, J. Phys.: Condens. Matter **21**, 395502 (2009).
[80] G. Onida, L. Reining, and A. Rubio, Rev. Mod. Phys. **74**, 601 (2002).
[81] N. Troullier and J. L. Martins, Phys. Rev. B **43**, 1993 (1991).